



Research Paper

Cite this article: Raptis SI, Ntokos K, Passia MT, Tourlouki K, Kehagias N, Kriezis EE, Yioultsis TV (2024) Ultra-thin and flexible microwave metasurface absorbers based on resistive patches. *International Journal of Microwave and Wireless Technologies* **16**(9), 1451–1464. <https://doi.org/10.1017/S1759078724001016>

Received: 13 April 2024
Revised: 3 April 2024
Accepted: 15 September 2024

Keywords:

metamaterial structures; metasurface absorbers; microwave absorbers; ultrathin and flexible metasurfaces

Corresponding author: Maria-Thaleia Passia;
Email: passiamg@ece.auth.gr

Ultra-thin and flexible microwave metasurface absorbers based on resistive patches

Savvas I. Raptis¹, Konstantinos Ntokos¹, Maria-Thaleia Passia¹ ,
Konstantina Tourlouki², Nikolaos Kehagias³,
Emmanouil E. Kriezis¹ and Traianos V. Yioultsis¹

¹School of Electrical and Computer Engineering, Aristotle University of Thessaloniki, Thessaloniki, Greece; ²Nanotypos, VEPE Technopoli Thessaloniki, Thessaloniki, Greece and ³Institute of Nanoscience & Nanotechnology, NCSR “Demokritos”, Athens, Greece

Abstract

We introduce a systematic approach for designing ultrathin, flexible, and polarization-insensitive metasurface absorbers (MSAs), suitable for aviation applications, such as radar cross-section reduction of unmanned aerial vehicles. Metal-backed resistive patches are arranged on a flexible polyethylene terephthalate substrate of thickness about 1/100 of the operating wavelength, classifying the absorbers as ultrathin. The ultralow weight of the proposed MSAs is crucial for the targeted aviation applications, to ensure airworthiness. A narrow-band uniform MSA is designed to achieve maximum absorption and serves as a starting point to synthesize a broadband and polarization-insensitive 3×3 absorber supercell. The non-uniform absorber is systematically designed by a fast semi-analytical method. The proposed absorbers have been fabricated and experimentally tested both on flat and cylindrical curved surfaces, with measurements being in very good agreement with the corresponding simulations, and corroborate the high absorption and broadband behavior of the proposed non-uniform ultrathin and flexible absorber.

Introduction

Over the recent years, great attention has been drawn in designing electromagnetic components based on metamaterials (MMs), which are artificial materials, engineered to attain bulk electromagnetic properties not readily found in nature [1]. Metasurfaces (MSs) are the two-dimensional extension of MMs and provide a fully planar, easy-to-fabricate platform for realizing electromagnetic components. MSs are synthesized by properly arranging identical or spatially varying subwavelength unit cells. Even though uniform MSs are used to achieve certain functionalities, the most appealing properties arise in non-uniform MS configurations. They are widely used in designing planar electromagnetic components such as antennas [2], lenses [3], filters [4], absorbers [5], with applications ranging from microwave to optical frequencies.

The concept of a perfect MM absorber was introduced by Landy *et al.* [6]. Specifically, a unit cell consisting of two MM elements, separately coupled to the incident electric and magnetic fields, was designed, attaining nearly perfect absorption. This work paved the way for designing and fabricating several MM, electromagnetic bandgap, and metasurface absorbers (MSAs), exhibiting wideband operation, polarization-insensitive behavior, and wide-angle performance [7–9]. The design of MSAs has been mainly carried out by equivalent-circuit models [10–13]. In these studies, the MSA is envisaged as a series resistor–inductor–capacitor resonating circuit [10]. By matching the total MSA impedance to that of free space, approximate values of the geometric parameters are obtained [11]. Lightweight and compact designs have gained considerable interest, especially in the context of radar cross-section (RCS) reduction or electromagnetic-interference shielding applications. Various microwave MSAs based on metal or all-dielectric resonators have been proposed in recent literature, with the reported thickness in most cases exceeding $\lambda_0/50$ [14–21], with notable exceptions such as [22], where an MSA of $\lambda_0/90$ thickness is synthesized by using μ -near-zero MMs in the form of vertically arranged double-layered spiral resonators. Certain ultrathin multiband absorbers have been also recently realized [23–26], which offer a narrow absorption band around each peak and are not conformal. Resistively loaded MS elements have been also introduced, to enhance the absorption bandwidth [10], in the form of a resistive film [27] or by inkjet-printing [8]. However, such ultrathin designs have not been yet reported in the X-band. Flexible RCS reduction devices based on graphene [28, 29] or indium tin oxide [30, 31] have been proposed over the last year but have a thickness of more than $\lambda_0/10$. Low weight, low profile, flexible, and broadband absorbers

© The Author(s), 2024. Published by Cambridge University Press in association with The European Microwave Association. This is an Open Access article, distributed under the terms of the Creative Commons Attribution licence (<http://creativecommons.org/licenses/by/4.0>), which permits unrestricted re-use, distribution and reproduction, provided the original article is properly cited.

would be beneficial to prominent aviation applications, such as the RCS reduction of unmanned aerial vehicles (UAVs), to ensure their airworthiness and structural integrity.

In this work, we provide a systematic approach for designing ultrathin and flexible, microwave MSAs, based on resistive metal patches of deep submicron thickness, with the MSA's thickness reasonably close to the estimated theoretical minimum by Rozanov's limit. The proposed MSAs are uniplanar, single-film, with easy single-step straightforward and cost-effective fabrication. Therefore, they provide an appealing choice for aviation applications, such as coating of curved UAV surfaces, without degrading the UAVs' aviation or drag performance. The ultra-thin MSAs lie on a metal-backed polyethylene terephthalate (PET) substrate of thickness $h = 0.27$ mm, corresponding to approximately $\lambda_0/100$ at $f = 11$ GHz. We initially propose a uniform MSA, based on a periodic arrangement of resistive patches. By the coupled-mode theory (CMT), we determine the necessary surface resistance and appropriate patch dimensions that maximize the absorption. To enhance the operational bandwidth of the uniform design, a non-uniform MSA is synthesized by properly arranging resistive patches of different size. The design of the non-uniform MSA is carried out by a systematic semi-analytical method, that quantifies mutual coupling between neighboring resistive patches. A supercell consisting of 3×3 patches provides a larger operating bandwidth of more than 68% absorption over a 1.2 GHz frequency range. The proposed uniform and non-uniform polarization-insensitive MSAs are fabricated and their performance is experimentally verified. Measurements and simulations of curved MSA samples show that our MSAs retain a satisfactory performance even for a large curvature.

Design of a uniform MSA

We design an ultrathin, polarization-insensitive MSA operating in the X-band in the vicinity of 11 GHz. A flexible low-loss PET substrate of thickness $h = 0.27$ mm is used, aiming at conformal lightweight designs. Based on the reported dielectric properties of PET [32–35], we consider a typical value of $\epsilon_r = 3$ and $\tan\delta = 0.009$ for the X-band. The MS is synthesized by a periodic arrangement of the metal-backed resistive square patch, which is depicted in Figure 1. The unit cell size D is chosen equal to 7 mm, which corresponds to about $\lambda_0/4$ at 11 GHz. The square patch size will be adjusted to provide a resonance at the desired operating frequency.

A CMT formulation is used to analyze and design the uniform MSA. Within the CMT framework, the resonator parameters are determined by eigenfrequency simulations, incorporating all loss mechanisms. CMT will be used to determine the appropriate values of both the patch size and the surface resistance R_s , that

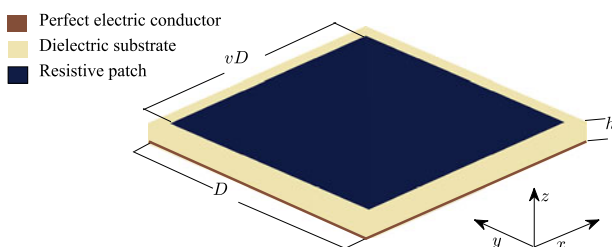


Figure 1. Metasurface absorber unit cell geometry of a metal-backed resistive square patch.

maximize the absorbance. CMT results will be validated against periodic full-wave finite-element method (FEM) simulations.

CMT model

The proposed MSA may be described by a temporal CMT (TCMT) model [36, 37]. The resonator comprising the MSA supports a single mode in the frequency range of interest, with the resonances being well-separated. The TCMT equation is of the following form [36]:

$$\frac{d\alpha(t)}{dt} = j\omega_t\alpha(t) - (\gamma_i + \gamma_e)\alpha(t) + \kappa^+s^+, \quad (1)$$

with $\alpha(t)$ being the resonator mode amplitude, $|\alpha(t)|^2$ the energy stored in the resonator, ω_t the real part of the resonant frequency with all losses included, s^+ the amplitude of incident wave, γ_i the intrinsic decay rate, accounting for dielectric and resistive losses and γ_e is the external decay rate, which in the case of a MSA, corresponds to radiation losses. The term $\kappa^+ = \sqrt{2\gamma_e}$ is the coupling coefficient between the resonator and the incident wave. A second equation, describing the de-excitation of the MSA, is also required:

$$s^- = cs^+ + \kappa^-\alpha(t), \quad (2)$$

in which s^- is the outgoing wave mode amplitude and $\kappa^- = \sqrt{2\gamma_e}$ is the coupling coefficient between the resonator and the outgoing wave. The parameter c accounts for the direct scattering process and is evaluated from the reflection imposed by the metal-backed substrate with appropriate referencing.

By combining the above equations and considering $\Gamma = s^-/s^+$ and $c = -1$, we obtain:

$$\Gamma = \frac{-j(\omega - \omega_t) - (\gamma_i - \gamma_e)}{j(\omega - \omega_t) + (\gamma_i + \gamma_e)}. \quad (3)$$

The absorbance $A = 1 - |\Gamma|^2$ is in turn calculated as [37]:

$$A = \frac{4\gamma_i\gamma_e}{(\omega - \omega_t)^2 + (\gamma_i + \gamma_e)^2}. \quad (4)$$

Perfect absorption is attained on resonance ($\omega = \omega_t$) and when the critical coupling condition is satisfied, with the intrinsic and external decay rates being equal, $\gamma_i = \gamma_e$. We note that c may assume any value depending on the choice of the reference plane, as long as the time-reversal symmetry condition is satisfied $c\kappa^{*-} = -\kappa^-$. The critical coupling condition is directly related to the impedance-matching condition, used in the absorber-related literature [11]. The normalized impedance Z/Z_0 is related to the coupling coefficient Γ as:

$$\frac{Z}{Z_0} = \frac{1 + \Gamma}{1 - \Gamma} = \frac{j(\omega - \omega_t) + \gamma_i}{j(\omega - \omega_t) + \gamma_e}. \quad (5)$$

The impedance matching condition, $Z = Z_0$, is satisfied when $\gamma_i = \gamma_e$, hence verifying the equivalence between the two conditions.

The decay rates, resonance frequencies, and Q-factors are calculated by eigenfrequency full-wave FEM simulations, within the COMSOL Multiphysics environment. As the proposed MSA is uniform, we model a single resonator, and enforce periodicity, by imposing periodic boundary conditions (PBCs) on the side boundaries of the MSA unit cell, i.e., along the x - and y -axes. The complex resonance angular frequency $\omega_{e/t}^c$ can be written in terms of its real

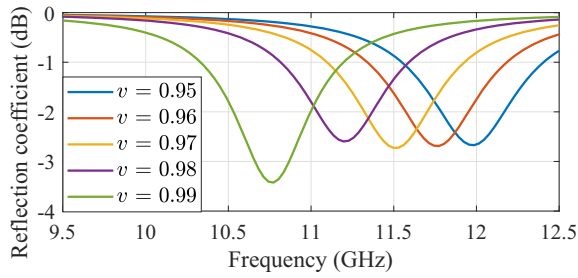


Figure 2. Reflection coefficient vs. frequency, varying the MSA unit cell filling factor v . Results are obtained by the CMT, with the patch considered as PEC.

part $\omega_{e/t}$ and the decay rate $\gamma_{e/t}$ as follows:

$$\omega_{e/t}^c = \omega_{e/t} + j\gamma_{e/t}. \tag{6}$$

The Q-factors are calculated as:

$$Q_{e/t} = \frac{\omega_{e/t}}{2\gamma_{e/t}}. \tag{7}$$

The resonance angular frequency in the absence of ohmic losses ω_e , Q-factor Q_e , and decay rate γ_e are extracted by performing an eigenfrequency full-wave simulation, accounting only for the external losses, which correspond to the resonator’s coupling to the incident wave. Hence, the metal surface is modeled as a perfect electric conductor (PEC), and the dielectric constant assumes a purely real value. The intrinsic resonator parameters cannot be directly calculated by an eigenfrequency full-wave simulation, as the external losses cannot be artificially switched off. To that end, we calculate the total decay rate γ_t , including all loss mechanisms, and retrieve the intrinsic decay rate γ_i using the relation:

$$\gamma_i = \gamma_t - \gamma_e. \tag{8}$$

Dielectric losses are taken into account by the complex dielectric constant of the PET substrate. The MSA patch is treated as a resistive ohmic sheet of zero thickness with a specified surface resistance value, imposed by a surface current density boundary condition. The lower layer of the substrate is modeled as PEC. The computational domain is truncated along the positive z -axis by a 1st order absorbing boundary condition.

By using the CMT, we can calculate the reflection coefficient of the MSA. As the patch is a symmetric structure, the response is identical for a normally incident TE- and TM-polarized wave, so we can calculate and illustrate the results for only one polarization. Our goal is to determine a suitable patch size, so that a resonance around 11 GHz will appear. We vary the unit cell filling factor v (Figure 1) in the range [0.95, 0.99] as in Figure 2 and treat the patch as PEC. As expected, as the unit cell filling factor increases, the resonant frequency decreases. A value of $v = 0.98$ sets the resonance close to 11 GHz.

As a next step, we determine the surface resistance R_s , that maximizes the absorption. We vary R_s in the range [0.05, 2] Ω/sq and calculate the external and intrinsic decay rates associated with each value of R_s . The intrinsic and external decay rates are depicted in Figure 3. The external decay rate is not influenced by R_s , as it depends solely on radiation losses. The intrinsic decay rate experiences a monotonic behavior, increasing along with R_s . We observe that the external and intrinsic decay rates are equal to each other, $\gamma_i = \gamma_e$, for surface resistance values around 1 Ω/sq , hence fulfilling the critical coupling condition [37, 38], and thus leading to

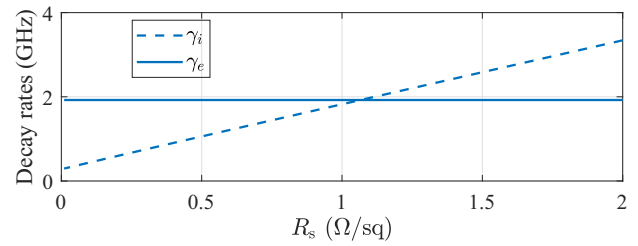


Figure 3. Intrinsic γ_i and external γ_e decay rates vs. the surface resistance.

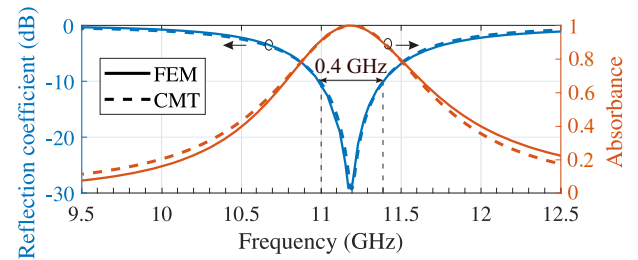


Figure 4. Reflection coefficient (dB) (left y-axis) and absorbance (right y-axis) vs. frequency for the proposed MSA. CMT calculations are compared against full-wave unit cell simulations.

maximum absorption. It is noted that the requirement for such low values of the surface resistance is strongly associated to the ultra-low thickness of the substrate, as also concluded in [10] and confirmed by the above simulations. In addition, such thickness values result in high filling factors, in order to place the resonance within the desired range.

Results

We verify the CMT results with spectral full-wave FEM simulations of the 3D MSA unit cell, by calculating the reflection coefficient and absorbance. The computational layout is identical to the previous case. Figure 4 shows the comparison between CMT and full-wave simulation results, for the chosen filling factor $v = 0.98$, and an excellent agreement is observed. Absorbance higher than 90% is attained within a frequency band of about 0.4 GHz, as denoted in Figure 4.

For a better assessment of absorption mechanisms, we also determine the contribution of resistive and dielectric losses, by post-processing the spectral 3D full-wave simulation results, with all losses included in the simulation. We thereby calculate the dissipated power due to resistive and dielectric losses and normalize with respect to the power of the incident wave. The power dissipated in the dielectric is calculated as $P_d = (1/2) \iiint_{V_d} \mathbf{J} \cdot \mathbf{E} dV = \pi f \tan \delta \epsilon_r \epsilon_0 \iiint_{V_d} |\mathbf{E}|^2 dV$, integrated over the volume of the dielectric and $\tan \delta$ the dielectric loss tangent. The power dissipated in the conductor is calculated as $P_c = (1/2) R_s \iint_{S_0} |\mathbf{J}_s|^2 dS$, integrated over the conductor’s surface, which is modeled by a surface current density boundary condition [39]. The results shown in Figure 5 indicate that resistive losses are the dominant loss mechanism, with a contribution of over 80% at the frequency of maximum absorption, while dielectric losses contribute less than 20%. The sum of the normalized dielectric and resistive losses is also shown, approaching unity at the resonance frequency.

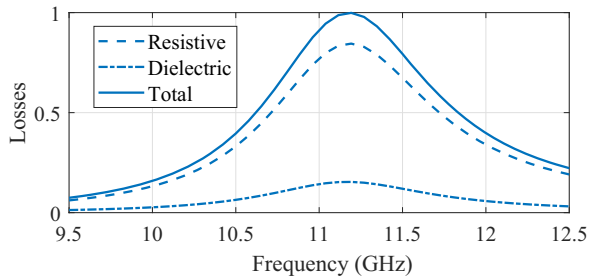


Figure 5. Contribution of different loss mechanisms.

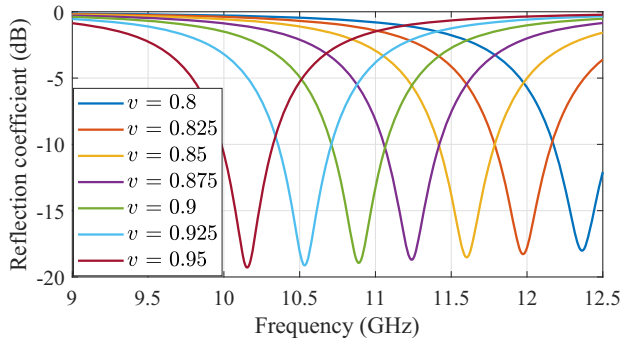


Figure 6. Parametric analysis of the reflection coefficient of the uniform MSA with period $D = 8.26$ mm and $R_s = 1 \Omega/\text{sq}$, varying the unit cell filling factor v . Results are obtained by the CMT.

Design of non-uniform MSAs for broadband operation

The analysis of the previous section reveals that a MS of uniform resistive patches with properly selected dimensions may effectively act as a narrowband resonant absorber. In this section, we aim at achieving broadband operation, hence we focus on non-uniform MSs, that combine patches of different size. We slightly increase the unit cell size from 7 mm to 8.26 mm, to accommodate a wider range of patch size values and thus a wider range of filling factor values, producing resonances in the frequency range of 10–12 GHz. We vary the filling factor v in the range $[0.8, 0.95]$, with the choice of $R_s = 1 \Omega/\text{sq}$. As expected, Figure 6 shows that the patch size and the resonant frequency vary inversely, according also to Figure 2. To determine the proper filling factor and patch configuration for each supercell element, we introduce a semi-analytical model that quantifies mutual coupling between neighboring elements. Initial values can subsequently serve as estimates for a fine-tuning of the non-uniform MSA realization. A similar method, based on the CMT, has been previously reported [40].

Semi-analytical approach quantifying mutual coupling

The MSA supercell is conceived as an array of N coupled elements, excited by an incident wave. Near-field coupling, quantified by the mutual impedance matrix, has been used to accurately model various MSs [41]. The upcoming analysis considers the mutual coupling between closest-neighboring absorbing elements, in terms of the surface currents [42].

By modeling the MS as a set of N coupled elements, the current flow at an arbitrarily selected reference point $\mathbf{r}'_{0,m}$ on the m th element, $I_m = I_m(\mathbf{r}'_{0,m})$, is expressed as [42]:

$$I_m = I_{0,m} + \sum_{\substack{n=1 \\ n \neq m}}^N H_{mn} I_n, \tag{9}$$

where $I_{0,m}$ is the current on $\mathbf{r}'_{0,m}$ when mutual coupling is neglected, and H_{mn} are mutual coupling coefficients. We note that \mathbf{r}'_m refers to the position vector of an arbitrary point located on the m th array element. Hence, (9) can be written as:

$$\mathbf{I} = \mathbf{H}^{-1} \mathbf{I}_0, \tag{10}$$

where $\mathbf{I} = [I_1 \ I_2 \ \dots \ I_N]^T$ and $\mathbf{I}_0 = [I_{0,1} \ I_{0,2} \ \dots \ I_{0,N}]^T$, with T denoting matrix transpose. The coefficient matrix \mathbf{H} , that quantifies near-field coupling, is expressed in the following form:

$$\mathbf{H} = \begin{bmatrix} 1 & -H_{12} & \dots & -H_{1N} \\ -H_{21} & 1 & \dots & -H_{2N} \\ \vdots & \vdots & \ddots & \vdots \\ -H_{N1} & -H_{N2} & \dots & 1 \end{bmatrix}. \tag{11}$$

The coefficients H_{mn} are considered to be non-zero only if resonators m and n are nearest neighbors. We also assume that the current distribution profile $i_n(\mathbf{r}'_n)$ is not affected by mutual coupling, i.e.,

$$\frac{I_n(\mathbf{r}'_n)}{I_n(\mathbf{r}'_{0,n})} = \frac{I_{0,n}(\mathbf{r}'_n)}{I_{0,n}(\mathbf{r}'_{0,n})} = i_n(\mathbf{r}'_n). \tag{12}$$

Hence, (10) may be used to calculate matrix elements H_{mn} and H_{nm} , provided that the currents $I_{0,m}$, $I_{0,n}$, which are assumed to be independent of mutual coupling, as well as the currents I_n and I_m , that account for mutual coupling, are already determined.

To determine each current $I_{0,n}$ and the current distribution profile i_n , we perform full-wave simulations under plane wave excitation, involving only the n th element of the array. Similarly, H_{mn} and H_{nm} are obtained, by a set of pairwise simulations considering elements m and n . All simulations are performed in a 3×3 supercell configuration, with the structure being excited in all cases by a normally incident plane wave, the computational domain is truncated by PBCs, and losses are included. We note that I_n may also represent a current density or a surface current density instead of a current, without essentially affecting the overall formulation. We will use the surface current density on the patches, as it obtained by COMSOL Multiphysics, with $\mathbf{r}'_{0,n}$ selected at the patch midpoint.

Validation of the semi-analytical approach on the 1×3 MSA supercell

We extend the uniform MSA design to form a 1×3 supercell, synthesized by patches of different size lying on the metal-backed PET substrate. Figure 7 illustrates the non-uniform MSA 1×3 supercell, with three unit cells placed along the x -axis and a single unit cell along the y -axis.

Based on the results of the parametric analysis of Figure 6, we choose the filling factor values $v_1 = 0.85$, $v_2 = 0.9$, and $v_3 = 0.95$ for the supercell design, aiming at absorption in the frequency range $[10, 11.5]$ GHz. The Ohmic loss of the n th element is calculated as [42]:

$$L_n = \frac{1}{2} \iint_S R_s |I_n(\mathbf{r}'_n)|^2 dS. \tag{13}$$

The R_s value used in (13) to determine the Ohmic losses is $R_s = 1 \Omega/\text{sq}$, as in Figure 6. By combining (12) and (13), we derive the

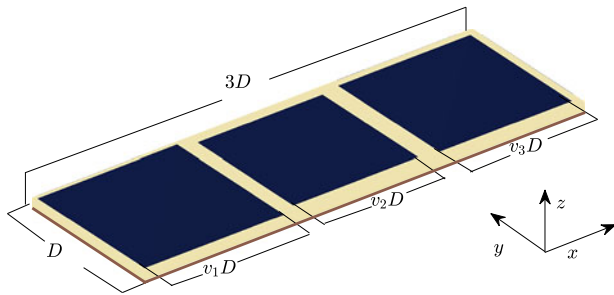


Figure 7. Configuration of the 1×3 non-uniform metasurface supercell.

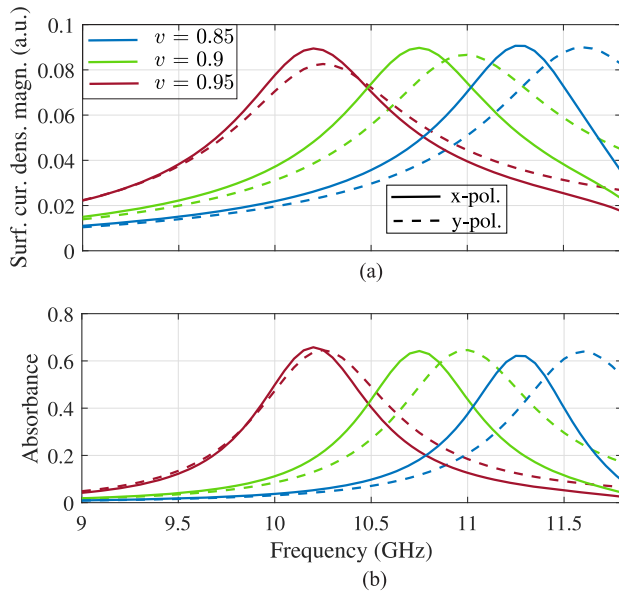


Figure 8. (a) Uncoupled surface current density $I_{0,n}$ magnitude and (b) absorbance vs. frequency, considering both x - and y -polarized incident waves for filling factor values $v_n = \{0.85, 0.9, 0.95\}$.

following expression

$$L_n = \frac{1}{2} \frac{\iint_S R_s |I_{0,n}(\mathbf{r}')|^2 dS}{|I_{0,n}|^2} |I_n|^2 = \frac{L_{0,n}}{|I_{0,n}|^2} |I_n|^2, \quad (14)$$

where $L_{0,n}$ is the Ohmic loss of the n th element in the absence of mutual coupling.

We perform both single-element and pairwise simulations, to determine the uncoupled $I_{0,n}$ and $L_{0,n}$ and coupled I_m and I_n currents, respectively. To obtain $I_{0,n}$ and $L_{0,n}$, we simulate the n th element, embedded within a 1×3 supercell environment, by a periodic full-wave solver. The center of each patch is set as the element's reference point $\mathbf{r}'_{0,n}$. The magnitude of the uncoupled surface current density $I_{0,n}$ is shown in Figure 8(a). Both an x - and y -polarized incident wave are considered for each filling factor value $v_n = \{0.85, 0.9, 0.95\}$. The absorbance of each element is also obtained from the corresponding reflection coefficient calculated by the periodic full-wave solver, as shown in Figure 8(b) for both polarizations. The absorbance of each element is different in the two polarizations, due to the asymmetric 1×3 supercell arrangement. The coupled I_m and I_n currents are obtained by pairwise simulation of the m th and n th elements. The coupling coefficient between elements #1 and #3 is non-zero, as they are first-nearest neighbors as well, considering an infinite periodic layout. Having

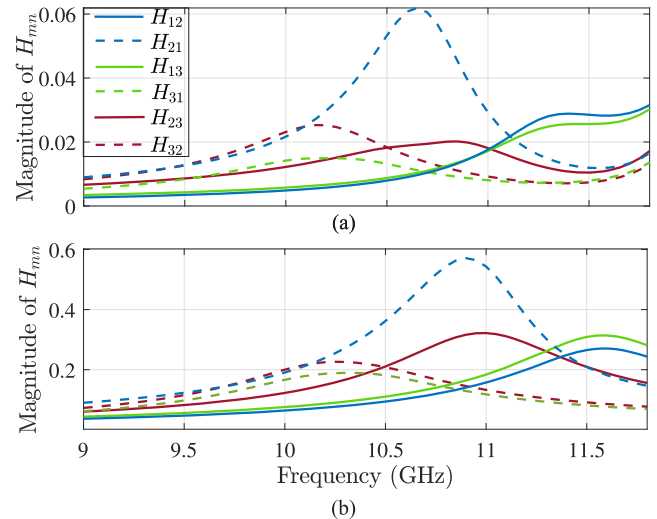


Figure 9. Magnitude of the calculated H_{mn} coefficients for an (a) x - and (b) y -polarized incident wave.

determined $I_{0,n}$, $I_{0,m}$, I_n , and I_m , we calculate the H_{mn} coefficients using (10). Figure 9(a) and (b) presents the magnitude of the calculated coefficients H_{mn} for both polarizations. All possible pairwise combinations are taken into account.

Once all H_{mn} and H_{nm} coefficients and the uncoupled currents $I_{0,n}$ are determined, we solve the system of equations (10) and calculate the currents I_n of the MS. The total Ohmic loss (i.e., the total absorbance) of the non-uniform MS is calculated by

$$L_{\text{tot}} = \sum_{n=1}^3 L_{0,n} \frac{|I_n|^2}{|I_{0,n}|^2}. \quad (15)$$

The overall semi-analytical approach described by equations (9)–(15) is, therefore, applied as follows: we restrict the possible resonator sizes to a small number of values, covering a reasonably wide range of resonant frequencies and we conduct full-wave simulations of both the individual resonators and all possible pairs of resonators in proximity, which form a very limited set of low-complexity simulations. The actual synthesis of the full MS will be, subsequently, performed via an exhaustive but fast search over all possible combinations among the limited preselected resonator sizes, based on the total absorbance by (15). We note that a full FEM model of a large sized MS, especially when employing all possible combinations of resonator placement, would result in an excessive number of simulations, which is computationally prohibitive.

For a thorough validation of the semi-analytical method, we compare the results against spectral full-wave simulations of an indicative 1×3 non-uniform MS shown in Figure 10, which will exhibit a very good agreement. As this MSA configuration is asymmetric, a different spectral response is observed according to polarization of the incident wave. It is evident, that a broader response is obtained, in case the electric field is oriented along the x -axis of supercell. The reflection coefficient is lower than roughly -5 dB in the range [10.05, 11.5] GHz, corresponding to a bandwidth of $\text{BW} = 1.41$ GHz, for the case of an x -polarized incident wave. A narrower bandwidth of about 1.1 GHz is attained for a y -polarized incident wave.

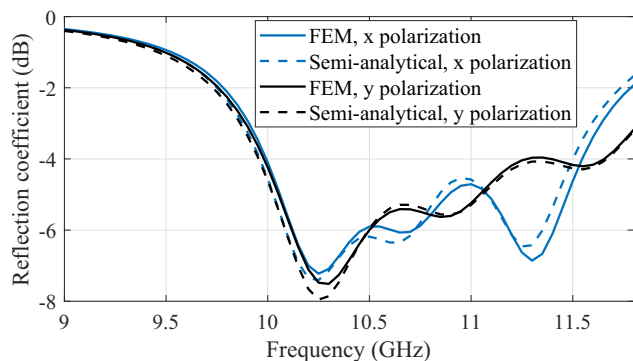


Figure 10. Reflection coefficient (dB) vs frequency, for the 1×3 non-uniform MSA supercell, considering both a x - and y -polarized normally incident plane wave. Semi-analytical results are compared against spectral full-wave results of the entire MSA and very good agreement is observed.

Synthesis of the non-uniform symmetric 3×3 MSA supercell

We extend the 1×3 MSA design to form a 3×3 non-uniform MSA configuration, with a polarization-insensitive response. The supercell dimensions are $3D \times 3D$, with $D = 8.26$ mm. The patch resonators are symmetrically placed with respect to the supercell main diagonal, to achieve polarization-insensitivity. Hence, six distinct patches of different size are used, each one having a different resonant frequency, as in Figure 11 (inset). We will employ a similar approximate analysis to identify the best possible resonators' layout for wideband absorption.

Similarly to the 1×3 structure, we calculate the \mathbf{H} coefficients of all permitted pairwise combinations, regarding size and position. We restrict the design only to filling-factor values $\nu = \{0.85, 0.9, 0.95\}$. The value $R_s = 1 \Omega/\text{sq}$ is used for the synthesis process. Due to the symmetric placement, only six values of ν are sought, within the above set. We conduct pairwise simulations in horizontal, vertical, and diagonal directions. Based on these simulations, we assign the H_{mn} coefficients, where m and n are the indices that map the patch to the 3×3 placement, hence $m, n = 1 \dots 9$. By considering all permitted combinations, of the position and filling factors of elements m and n , we calculate the absorption by (15) and select the best combination. We note that the required pairwise simulations are drastically reduced, due to the symmetric placement of the patches, the restriction to only three filling-factor values and by considering only first-nearest neighbors. The aforementioned systematic design process is also very time- and memory-efficient, compared against parametric spectral full-wave simulations of the entire supercell. The parameter set resulting from the semi-analytical synthesis approach is $\nu_1 = 0.95$, $\nu_2 = 0.9$, $\nu_3 = 0.85$, $\nu_4 = 0.95$, $\nu_5 = 0.85$, and $\nu_6 = 0.9$. Semi-analytical and full-wave simulation results of the MSA reflection coefficient are presented in Figure 11. As the 3×3 MSA is a symmetric structure, the response is identical for a normally incident TE- and TM-polarized wave, so we can calculate and illustrate the results for only one polarization. A very good agreement is attained between the two methods.

The adopted parameter set, obtained by the semi-analytical approach, serves as a starting point for the fine-tuning process. We use a genetic-algorithm optimization in conjunction with full-wave simulations. The average reflection coefficient in the range 10–12 GHz is chosen as the fitness function, which we try to minimize, aiming at lower reflection coefficient values across an even broader frequency range. Apart from the filling factors we also

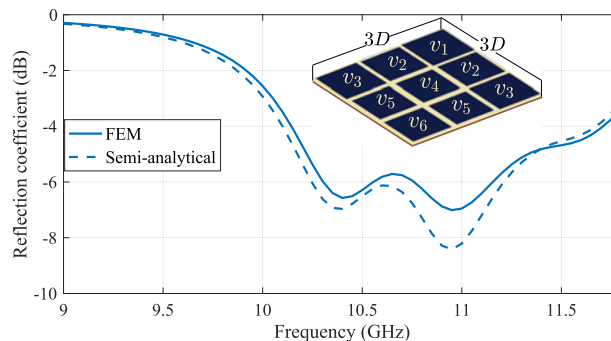


Figure 11. Reflection coefficient (dB) vs frequency, for the 3×3 non-uniform MSA supercell, obtained by the semi-analytical and full-wave simulation results of the entire MSA. The 3×3 supercell with all filling factors are shown as an inset.

allow for small variations in the unit cell size and the surface resistance, thus providing additional degrees of freedom, which may lead to an even more optimized configuration. By enforcing lower and upper bounds on the parameters, we help the algorithm converge toward a more optimized parameter set faster, by searching in a limited parameter space. The following finalized design parameters are: $D = 8.275$ mm, $R_s = 0.34 \Omega/\text{sq}$, $\nu_1 = 0.957$, $\nu_2 = 0.893$, $\nu_3 = 0.934$, $\nu_4 = 0.854$, $\nu_5 = 0.861$, and $\nu_6 = 0.889$.

We also provide a physical interpretation of the ultra-low substrate thickness on R_s values, tuned for high absorption in the case of the 3×3 non-uniform MSA. Hence, we determine the value of R_s that fulfill the critical coupling condition for each one of the supported modes of the supercell, as follows. A periodic eigenfrequency analysis of the 3×3 supercell is carried out, identifying all supported modes of the configuration, in the frequency range of interest [10, 12] GHz. Eighteen modes are supported in this range, pairwise degenerate. Nine distinct modes are plotted in Figure 12. It is evident that different modes correspond to different combinations of excited patches. The resonance frequencies of the supercell modes differ from those of individual resonators due to the coupling between neighboring elements. The real part of the eigenfrequency of each supported supercell mode is reported in Table 1, considering $R_s = 1 \Omega/\text{sq}$, while the resonance frequencies of individual resonators are $f_1 = 10.423$ GHz, $f_2 = 11.069$ GHz, $f_3 = 10.63$ GHz, $f_4 = 11.479$ GHz, $f_5 = 11.413$ GHz, $f_6 = 11.185$ GHz. By direct inspection of Table 1, one can correlate the supercell resonant frequencies with those of individual resonators. Clearly, there are observable shifts due to the inter-resonator coupling. By varying the surface resistance R_s , the imaginary part of the eigenfrequency, which is related to the MS losses, also changes. Meanwhile, the real part of the eigenfrequency experiences a slight shift.

We calculate the intrinsic and external decay rates, γ_i and γ_e , respectively, related to each of the nine supported modes of the 3×3 non-uniform MS supercell, varying the surface resistance value R_s in the range $[0.05, 1] \Omega/\text{sq}$. As in the case of the uniform MS, the external decay rate of each mode remains constant, as it only depends on leakage or radiation losses, whereas the intrinsic decay rate experiences a monotonic behavior, increasing along with R_s . In contrast to the uniform MS, which experiences critical coupling, $\gamma_i = \gamma_e$, when $R_s = 1 \Omega/\text{sq}$, the 3×3 non-uniform MS requires lower values of R_s , i.e., below $0.2 \Omega/\text{sq}$, to achieve critical coupling, as shown in Figure 12 for modes #1 and #4.

We confirm the findings of the eigenfrequency analysis of the MS supercell, by calculating the reflection coefficient of the 3×3

Table 1. Real part of the eigenfrequency (GHz) of each supported mode of the 3 × 3 non-uniform MS supercell

f_1	f_2	f_3	f_4	f_5	f_6	f_7	f_8	f_9
10.339	10.612	10.748	10.981	11.14	11.178	11.388	11.487	11.573

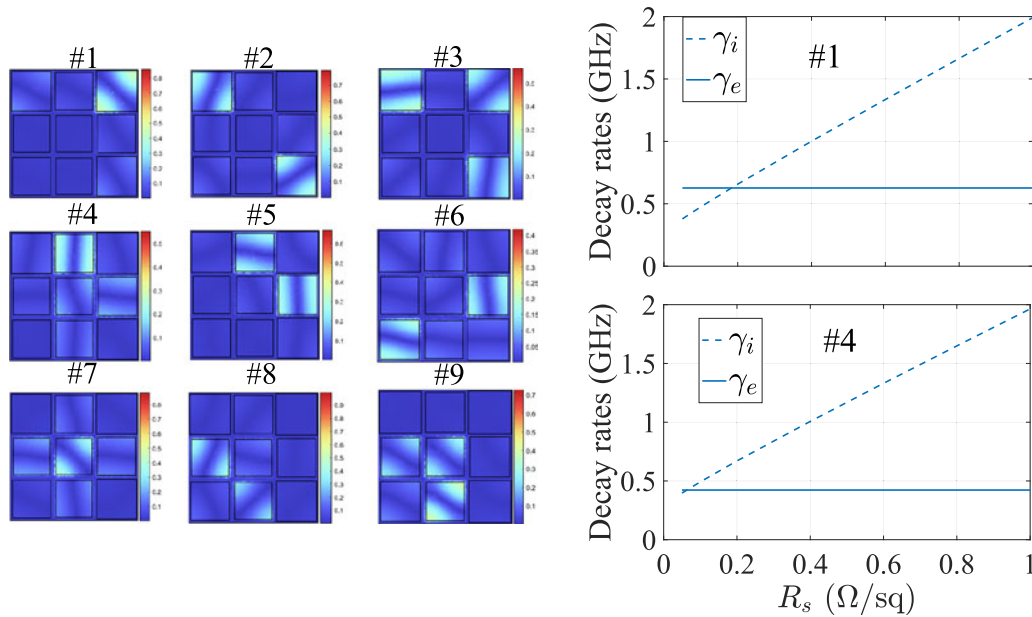


Figure 12. Normalized electric field norm at mid-substrate of the supported modes of the 3 × 3 non-uniform MS supercell. Intrinsic (γ_i) and external (γ_e) decay rates are shown for modes #1 and #4, varying R_s .

non-uniform MS, by employing the full-wave periodic solver and considering three different R_s values, 0.05, 0.34, and 1 Ω/sq. The results corresponding to a normally incident plane wave are presented in Figure 13, for the filling factors and unit cell size obtained by the optimization process. We observe that lower values of R_s lead to sharper and more pronounced resonances. Specifically, in case of $R_s = 0.05 \Omega/sq$ four resonances are visible, in case of $R_s = 0.34 \Omega/sq$ we observe three resonances and $R_s = 1 \Omega/sq$ results in a smoother response. Based on the preceding discussion, the resonances are in all cases nine. However, the lower quality factors associated with higher R_s values, results in resonances being merged and a broadband response. The first two cases have a very similar performance. This claim is verified by the average reflection coefficient, equal to -4.4 dB and -4.6 dB, for $R_s = 0.34 \Omega/sq$ and $0.05 \Omega/sq$, respectively. We choose $R_s = 0.34 \Omega/sq$ for the non-uniform MS configuration, as it provides an acceptably large bandwidth with reasonably low reflection coefficient values. The reflection coefficient is retained lower than -5 dB in the frequency range of [10.2,11.4] GHz, corresponding to a bandwidth of BW = 1.2 GHz. The 3 × 3 non-uniform MS is associated with a higher bandwidth compared to the uniform configuration, with a 50% relative improvement, similar to that of the 1 × 3 non-uniform MS, while offering a polarization-insensitive design.

Performance evaluation based on the Rozanov limit

The performance of the MSA may be further assessed by calculating the Rozanov limit [43], which provides an estimation of the largest possible bandwidth that may be attained, considering a pre-determined thickness and reflectance of the absorber. Specifically, the maximum reflection coefficient ρ_0 that may be attained within

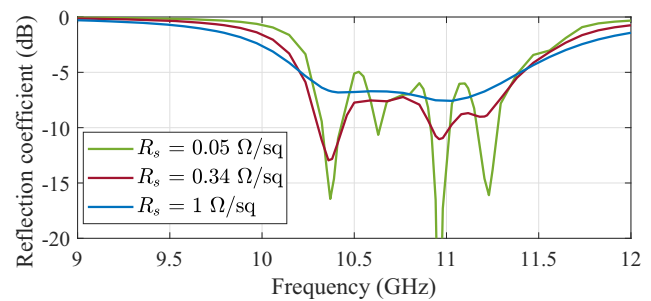


Figure 13. Reflection coefficient (dB) vs frequency, for the 3 × 3 supercell, under normal incidence, for $R_s = 0.05, 0.34,$ and $1 \Omega/sq$.

$\Delta\lambda = \lambda_{\max} - \lambda_{\min}$ is related to the relative magnetic permeability μ_i and thickness d_i of each layer i of the absorber through the following inequality [43]:

$$|\ln \rho_0| \Delta\lambda \leq 2\pi^2 \sum_i \mu_i d_i. \tag{16}$$

As the proposed 3 × 3 non-uniform MSA consists of a single nonmagnetic layer, inequality (16) is transformed into

$$|\ln \rho_0| \Delta\lambda \leq 2\pi^2 d. \tag{17}$$

Hence, the minimum theoretical value of the absorber thickness d_{\min} is calculated as

$$d_{\min} = \frac{|\ln \rho_0| \Delta\lambda}{2\pi^2}. \tag{18}$$

According to the results of the non-uniform 3 × 3 MS (Figure 13), the reflection coefficient Γ_0 is less than -5 dB

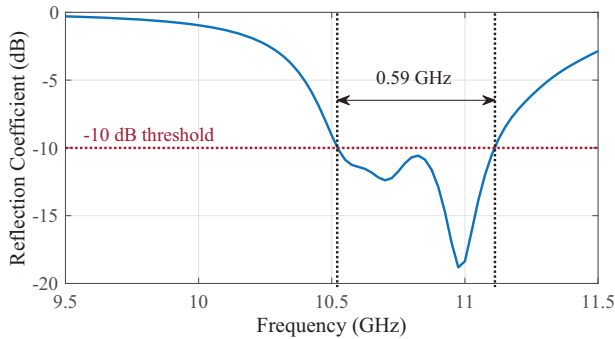


Figure 14. Reflection coefficient (dB) vs frequency, for the 3×3 supercell, under normal incidence, for the non-uniform MSA that achieves 90% absorption.

within the frequency range [10.2, 11.4] GHz. The minimum substrate thickness d_{\min} is thus calculated equal to 0.09 mm, i.e., about 0.1 mm.

Inequality (16) provides the ultimate minimum thickness that may be attained. A strict estimation of the minimum was calculated above, considering the reflection coefficient Γ_0 less than -5 dB within the frequency range [10.2, 11.4] GHz, and 0 dB elsewhere. A more realistic calculation of the minimum thickness, may be calculated, based on the following inequality [43]:

$$\left| \int_0^\infty \ln |\rho(\lambda)| d\lambda \right| \leq 2\pi^2 \sum_i \mu_i d_i, \quad (19)$$

keeping in mind that

$$|\ln \rho_0| \Delta\lambda \leq \left| \int_0^\infty \ln |\rho(\lambda)| d\lambda \right|. \quad (20)$$

By limiting the integral within $\lambda_{\min} = 0.025$ m and $\lambda_{\max} = 0.033$ m, corresponding to a frequency range of [9, 12] GHz, we estimate the minimum thickness required to obtain the reflection coefficient of the $R_s = 0.34 \Omega/\text{sq}$ case of Figure 13, found to be equal to $d_{\min} = 0.19$ mm. The realized substrate thickness of the 3×3 MSA is $h = 0.27$ mm, which is reasonably close to the above estimated theoretical minimum. It is also noted that higher absorption levels, in the order of 90%, may appear in the literature but this most commonly refers to significantly thicker substrates. For ultrathin MSAs, especially for aviation applications, with a thickness in the order of $\lambda/100$, lower absorption levels are naturally anticipated for reasonably wideband operation. This is dictated by Rozanov's limit, demonstrating the trade-off between substrate thickness, minimum absorbance, and operating bandwidth. Therefore, for the particular choice of -5 dB reflection, a chief advantage of the proposed design is that the realized thickness of 0.27 mm is reasonably close to the theoretical minimum of 0.19 mm, which is nevertheless very hard to approach. Obviously, the level of absorption is a matter of an application-dependent choice and higher levels could be attained either by thicker substrates or within narrower bandwidths. We have confirmed via extensive simulations that the proposed MSA design framework can achieve a 90% absorption level (corresponding to -10 dB reflection reduction), naturally over a narrower bandwidth. We present in Figure 14 such a design with design parameters $D = 8.275$ mm, $R_s = 0.4 \Omega/\text{sq}$, $\nu_1 = 0.930$, $\nu_2 = 0.900$, $\nu_3 = 0.880$, $\nu_4 = 0.885$, $\nu_5 = 0.875$, and $\nu_6 = 0.850$, which achieves a 90% absorption level over 0.59 GHz (5.5% fractional bandwidth). We have to note that the -10 dB design delivers a narrower -5 dB reflection bandwidth compared to the original

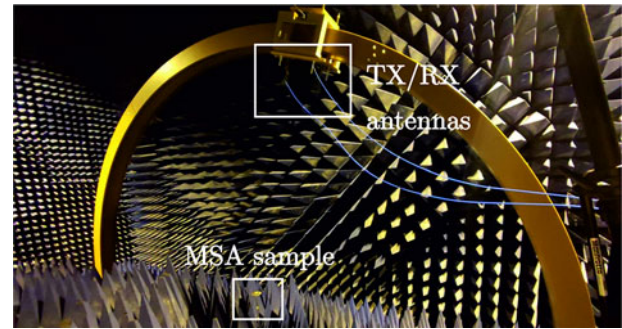


Figure 15. Experimental setup of the MSA. Both receiving and transmitting horn antennas are attached to a wagon, that moves along an arch. The MSA sample is placed at far-field distance at the center of the arch.

one, i.e., 0.9 GHz instead of 1.2 GHz. Therefore, we have specifically opted for an increased -5 dB bandwidth, accepting absorption levels of 68% (corresponding to -5 dB maximum reflection), since these were deemed sufficient for our application. It is emphasized that via the proposed approach we can always trade off bandwidth for absorption, depending on the application.

Experimental verification

The designed absorbers have been fabricated and their performance is experimentally verified. An ultrathin aluminum layer of thickness $t_{\text{Al}} = 100$ nm is evaporated (via electron beam evaporation) over a $270 \mu\text{m}$ thick PET substrate via a metallic stencil mask for the realization of discrete patches, while the device sealing is ensured by coating with a UV curable monomer, which acts as a protective layer. We have measured aluminum's electric conductivity approximately equal to $\sigma_{\text{Al}} = 2.95 \times 10^7$ S/m, by means of 100 nm aluminum samples deposited on top of a $96 \mu\text{m}$ PET layer, using a vector network analyzer and WR-90 waveguide components. A transmission-line model is used, with aluminum introduced as a shunt resistance and the theoretical transmission is compared against the measured one, to deduce aluminum's electric conductivity. A satisfactory agreement is observed, when aluminum's electric conductivity is set to about 80% of its nominal bulk value [44]. As aluminum's skin depth at the center frequency of the X-band is $\delta_{\text{Al}} = 926$ nm $\gg t_{\text{Al}}$, we use the quasi-static approximation $R_s = 1/(\sigma_{\text{Al}} t_{\text{Al}})$ [10], to relate aluminum's surface resistance to the corresponding conductivity and thickness. A surface resistance of about $R_s = 0.34 \Omega/\text{sq}$ is obtained. Higher values of the surface resistance, around $R_s = 1 \Omega/\text{sq}$, could be achieved by employing an aluminum layer of thickness $t_{\text{Al}} \approx 35$ nm, however values around 100 nm were preferred to facilitate the fabrication process.

MSA samples of the uniform and non-uniform designs are experimentally tested within an anechoic chamber. The experimental setup consists of a receiving and transmitting Narda 640 16.5 dB standard gain X-band horn antenna, attached to a wagon, moving along an arch. Both horn antennas point at the MSA sample, which is placed at far-field distance at the center of the arch, as shown in Figure 15. Measurements are obtained by using a signal generator and a spectrum analyzer. We consider TE polarization of the incident wave, and provide measurements at normal incidence. All measurements are compared against measurements of a metal plate of identical dimensions and shape, quantifying the relative RCS reduction offered by the MSA.

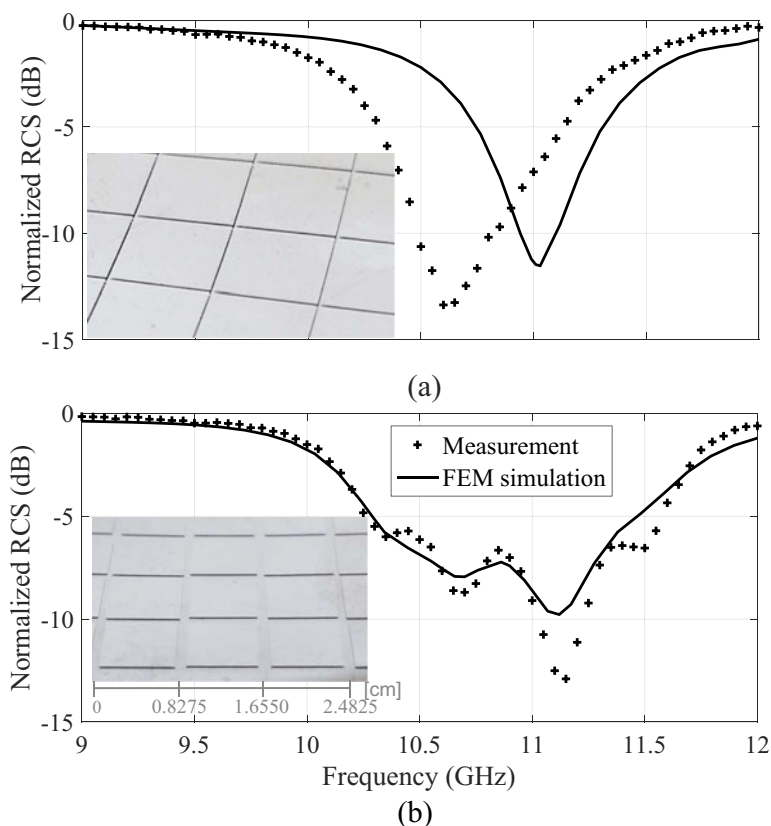


Figure 16. Normalized RCS (dB) vs. frequency (GHz) for the (a) uniform 10×10 and (b) non-uniform 9×9 MSA sample, considering a normally incident TE-polarized wave. The fabricated MSA sample is shown as an inset.

Uniform MSA variation

We provide a comparison between experimental and scattered-field full-wave simulation results of the uniform MSA sample, comprised by a 10×10 repetition of the MSA unit cell. The surface resistance is set to $R_s = 0.34 \Omega/\text{sq}$ in the simulations as well. Figure 16(a) presents the normalized monostatic RCS, along with a photograph of the fabricated MSA sample, shown as an inset. Good agreement between measurements and simulations is observed, with the resonance downshifted by about 0.4 GHz in the measurements. An RCS reduction of at least 5 dB is achieved within a 0.85 GHz band, according to the experimental results.

Non-uniform MSA variation

A comparison between experimental and scattered-field full-wave simulation results is also carried out for the 9×9 non-uniform MSA sample, i.e., a 3×3 repetition of the 3×3 supercell. We set $R_s = 0.34 \Omega/\text{sq}$ in this case as well. Figure 16(b) shows the normalized monostatic RCS for both cases, along with the corresponding photograph of the fabricated sample, as an inset. Experimental results are in very good agreement with the simulations. An RCS reduction of at least 5 dB is attained, with respect to a metal plate of identical dimensions, for a 1.2 GHz and 1.3 GHz, according to simulations and measurements, respectively. Even though experimental results point to a slightly greater bandwidth, both verify the broader spectral response of the non-uniform MSA design.

We also present measurements of normalized RCS for oblique incidence, where absorption properties will be shown to remain at significant levels. This is despite that the MSA has been designed for maximum absorption at normal incidence, since in applications such as coating of aerial vehicles, the electromagnetic signature is mostly pronounced at normal incidence and considerably lower

at oblique angles. Therefore, we provide simulations and measurements of the non-uniform MSA under oblique incidence up to 60° , for both TE and TM polarization, in Figure 17. The measurements now refer to bistatic RCS toward the specular direction, for various angles of incidence, which has been normalized with respect to the RCS of an equally sized metal plate for the same directions of incident and scattered waves. It is observed that for the TE case the performance gradually degrades as the angle of incidence increases, still achieving at 20° a normalized RCS of less than -5 dB within a 1.16 GHz bandwidth. For the TM polarization, a good performance is essentially retained for angles up to 60° , with normalized RCS of less than -5 dB being achieved within a 1.07 GHz bandwidth at the highest angle. Poorer angular stability under TE polarization is anticipated for ultrathin MSAs, as the free-space impedance will increase along with the incident angle, whereas the MSA's input impedance will remain almost equal to that of normal incidence, leading to impedance mismatch, and consequently a degraded performance. Angular stability is expected under TM polarization, as both the input and free-space impedance gradually decrease, and hence they remain well-matched [11].

It is noted that the measured RCS values cannot directly translate into absorbance, though they are highly correlated. This is due to the fact that the sample dimensions are relatively small, and thus, the bistatic RCS does not coincide with the reflection coefficient of the infinite MSA. In the latter case, the absorbance is directly calculated as $A = 1 - |R|^2$.

Curved MSAs

As our MSAs are intended for achieving RCS reduction in aviation applications, we also assess our MSA's performance when mounted on a cylindrical curved surface. Specifically, we place both

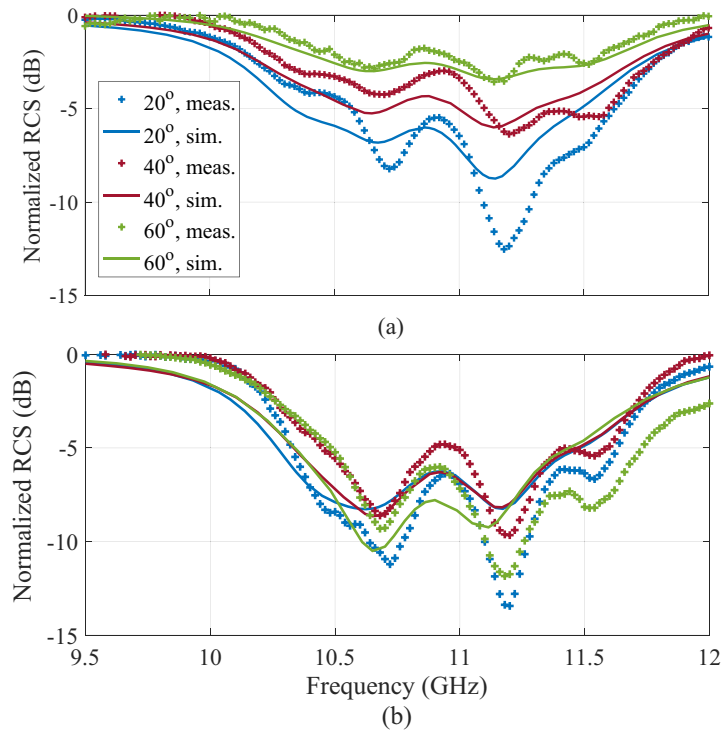


Figure 17. Normalized RCS (dB) vs. frequency (GHz) for the non-uniform 9×9 MSA sample, considering an obliquely incident (a) TE- and (b) TM-polarized wave. Incident angles of up to 60° are considered.

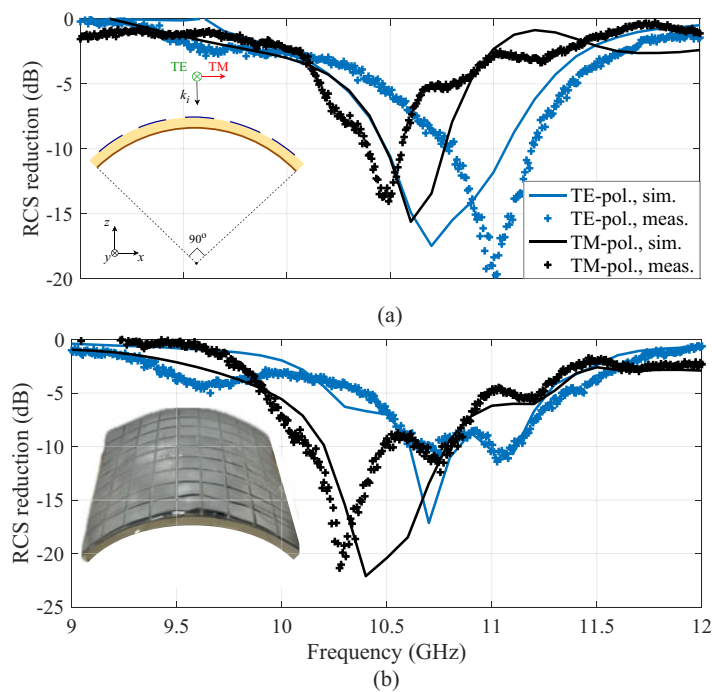


Figure 18. Normalized RCS (dB) vs. frequency (GHz) for the (a) uniform and (b) non-uniform curved MSA sample for a normally incident TE- and TM-polarized wave. The considered curvature, corresponding to a 90° arc, as well as a photograph of the curved sample are included as insets.

the uniform and non-uniform MSAs on a cylindrical surface of a 90° arc, as depicted in the insets of Figure 18, which show the curvature and a photo of the mounted MSA sample. We calculate and measure the normalized RCS of the curved MSA samples, with respect to a PEC sample of identical dimensions and curvature, for both a TE- and TM-polarized normally incident plane wave in the range 9–12 GHz. The measured and simulated RCS reduction is shown in Figure 18 for the uniform and non-uniform

MSAs, and a satisfactory agreement is obtained. The 68% absorption bandwidth is 1 GHz and 0.63 GHz for the uniform MSA under TE and TM polarization, according to simulations. Similarly, for the non-uniform MSA, the 68% absorption bandwidth is 1 GHz and 1.3 GHz for TE and TM polarization. We conclude that even for the considered relatively large curvature, which is considerably greater than most typical curvatures of UAV constituent surfaces, i.e., UAV wings, our MSAs achieve a performance very close to

Table 2. Comparison between the proposed uniform and non-uniform 3×3 MSAs and MSAs from the literature in the X-band

MSA design	68% absorption BW (GHz)	80% absorption BW (GHz)	f_c (GHz)	h (λ_0)	Polarization insensitive	Flexible	TE-pol. (oblique) 68% BW (GHz)	TM-pol. (oblique) 68% BW (GHz)	Dominant loss mech.
[28] (m)	12	10	12	0.1330		✓	$10, \theta \leq 55^\circ$	$10, \theta \leq 55^\circ$	Resistive
[8] (m)	24.35	23	10.05	0.1300	✓	✓	$28, \theta \leq 45^\circ$	$28, \theta \leq 45^\circ$	Resistive
[45] (s)	5.86	5	12.5	0.1000	✓		$7, \theta \leq 30^\circ$	$6, \theta \leq 45^\circ$	Dielectric
[46] (m)	10.5	10.5	15	0.1000	✓	✓	N/A	N/A	Resistive
[18] (s)	>4	4	10.2	0.0535	✓	✓	$4, \theta \leq 30^\circ$	$4, \theta \leq 30^\circ$	Dielectric
[47] (m)	1.3	1.1	9.25	0.0360	✓	✓	$0.6, \theta \leq 60^\circ$	N/A	Resistive
[24] (s)	0.2	0.1	10	0.0330	✓		$<0.1, \theta \leq 40^\circ$	$<0.1, \theta \leq 40^\circ$	Dielectric
[48] (s)	0.5	0.2	10.25	0.0205	✓		N/A	N/A	Dielectric
Our work (m)	0.8	0.5	10.6	0.0097	✓	✓	N/A	N/A	Resistive
Our work (s)	1.2	0.8	10.75	0.0097	✓	✓	$0.13 \text{ \& } 0.3 \theta=40^\circ$	$1.07 \theta=60^\circ$	Resistive

that of a flat sample. Specifically, the non-uniform MSA achieves a slightly increased 68% absorption bandwidth of 1.3 GHz instead of 1.2 GHz for the TM polarization, while it accomplishes a somewhat narrower bandwidth of 1 GHz for the TE polarization. Therefore, the curved MSA essentially retains its competitive performance, regarding absorption and bandwidth properties, both for TE and TM polarization, even in the case of a considerable curvature.

Comparison between the proposed MSAs with MSAs from the literature

A comparison between the proposed uniform and non-uniform 3×3 MSA and other mostly thin, X-band MSAs, reported in the literature, is carried out and presented in Table 2. The comparison is performed in terms of the (i) bandwidth, where absorption is above 68% (the corresponding reflection coefficient is below -5 dB), (ii) bandwidth, where absorption is above 80% (the corresponding reflection coefficient is below approximately -7 dB), (iii) center operating frequency f_c , (iv) substrate thickness h in terms of the free-space wavelength, (v) polarization insensitivity, (vi) flexibility, (vii) bandwidth, where absorption is above 68% for an obliquely incident TE wave, and (viii) bandwidth, where absorption is above 68% for an obliquely incident TM wave and (ix) dominant loss mechanism. The bandwidth where absorption is above 68% or 80% under normal or oblique incidence is inferred from simulation results (s) or measurements (m). N/A denotes that the information is not available. Table 2 is sorted in terms of the substrate thickness in descending order, i.e., from the thicker to the thinner substrate. We show that our work has an ultrathin substrate, ranking best, while it is also flexible and polarization insensitive and retains angular stability for angles up to at least 30° . We also verify that thicker substrates lead to an overall higher absorption bandwidth, for absorbers assembled by identical materials. It is also evident, that the incorporation of resistive losses greatly enhances the absorption bandwidth. The dominant absorption mechanism of the configurations proposed in [24, 48] are dielectric losses, with copper losses having a limited effect in the X-band. Even though the substrate thickness of such absorbers is about two to three times greater than the substrate thickness used in our design, our uniform MSA exhibits a greater bandwidth compared against the aforementioned designs, and is additionally flexible. We note that there are other flexible and polarization-insensitive

MSAs, however, as shown in Table 2 they are considerably thicker, which renders our MSA more suitable for the targeted aviation applications.

Conclusions

Ultrathin, flexible, polarization-insensitive microwave MSAs for the X-band, based on resistive patches, have been presented in this work, with resistive losses being the dominant absorption mechanism. The ultrathin and flexible MSA design process starts by selecting the filling factor and the surface resistance value to meet the critical coupling condition, so that maximum absorption is obtained at the targeted frequency. To achieve a higher absorption bandwidth, a 3×3 symmetric supercell has been designed, by assembling patches of different size. The appropriate dimensions and layout have been determined at the initial design phase, by using a semi-analytical method. The non-uniform MSA exhibits a 5 dB RCS reduction for a 1.2 GHz bandwidth. The performance of the 3×3 non-uniform MSA is close to the performance dictated by the Rozanov limit. The MSAs are fabricated, with the resistive patches based on 100 nm aluminum layers, that are patterned using electron beam evaporation via a metallic stencil mask. Measurements in an anechoic chamber and scattered-field full-wave simulations of the finite flat MSA samples corroborate the performance of the uniform and non-uniform designs, with a satisfactory agreement achieved between them. Corresponding simulations and measurements of curved MSA samples are also conducted for a relatively large 90° curvature, proving that the MSA retains an overall satisfactory and acceptable performance, even in a more curved configuration than most UAV constituent surfaces. The proposed MSAs provide an appealing choice for microwave RCS reduction applications, due to their ultrathin, lightweight, and compact characteristics. The MSAs are manufactured by widely available and inexpensive materials as well as an one-step manufacturing process of aluminum evaporation, which is fast, well-controlled, high-precision, and fully scalable to larger structures. As the PET films are flexible and conformal, the proposed designs can serve as an excellent choice for curved surfaces, such as those of UAVs or other aviation applications.

Acknowledgements. This work was implemented within the project "RADAERO-Innovative Composite Materials for the Drag and Electromagnetic Signature Reduction for Applications in Aviation" (project

code: T6YBII-00042), which was financially supported by the European Regional Development Fund, Partnership Agreement for the Development Framework (2014–2020), co-funded by Greece and the European Union in the framework of the OPERATIONAL PROGRAMME: “Competitiveness, Entrepreneurship and Innovation 2014–2020 (EPAN EK),” Nationwide Action: “Industrial Materials.” The publication of the article in OA mode was financially supported by HEAL-Link.

Author contributions. S. I. Raptis, K. Ntokos and M.-T. Passia are co-first authors.

Competing interests. The authors declare none.

References

- Holloway CL, Kuester EF, Gordon CA, O'Hara J, Booth J and Smith DR (2012) An overview of the theory and applications of metasurfaces: The two-dimensional equivalents of metamaterials. *IEEE Antennas and Propagation Magazine* 54(2), 10–35.
- Faenzi M, Minatti G, Gonzalez-Ovejero D, Caminita F, Martini E, Della Giovampaola C and Maci S (2019) Metasurface antennas: new models, applications and realizations. *Scientific Reports* 9, 10178–1–10178–14.
- Azad AK, Efimov AV, Ghosh S, Singleton J, Taylor AJ and Chen HT (2017) Ultra-thin metasurface microwave flat lens for broadband applications. *Applied Physics Letters* 110(22), 224101–1–224101–6.
- Ortiz JD, Baena JD, Losada V, Medina F, Marques R and Araque Quijano JL (2013) Self-complementary metasurface for designing narrow band pass/stop filters. *IEEE Microwave and Wireless Components Letters* 23(6), 291–293.
- Liu X, Fan K, Shadrivov IV and Padilla WJ (2017) Experimental realization of a terahertz all-dielectric metasurface absorber. *Optics Express* 25(1), 191–201.
- Landy NI, Sajuyigbe S, Mock JJ, Smith DR and Padilla WJ (2008) Perfect metamaterial absorber. *Physics Review Letters* 100(20), 207402–1–207402–4.
- Elsharabasy A, Bakr M and Deen MJ (2020) Wide-angle, wide-band, polarization-insensitive metamaterial absorber for thermal energy harvesting. *Scientific Reports* 10, 16215–1–16215–10.
- Assimonis SD and Fusco V (2019) Polarization insensitive, wide-angle, ultra-wideband, flexible, resistively loaded, electromagnetic metamaterial absorber using conventional inkjet-printing technology. *Scientific Reports* 9, 12334–1–12334–15.
- Assimonis SD, Kollatou TM, Yioultis TV and Antonopoulos CS (2014) Absorbing surfaces using EBG structures. *IEEE Transactions on Magnetics* 50(2), 7004704–1–7004704–4.
- Costa F, Monorchio A and Manara G (2010) Analysis and design of ultra thin electromagnetic absorbers comprising resistively loaded high impedance surfaces. *IEEE Transactions on Antennas and Propagation* 58(5), 1551–1558.
- Costa F, Genovesi S, Monorchio A and Manara G (2013) A circuit-based model for the interpretation of perfect metamaterial absorbers. *IEEE Transactions on Antennas and Propagation* 61(3), 1201–1209.
- Costa F, Monorchio A and Manara G (2016) Theory, design and perspectives of electromagnetic wave absorbers. *IEEE Electromagnetic Compatibility Magazine* 5(2), 67–74.
- Hossain MI, Nguyen-Trong N and Sayidmarie KH (2020) Equivalent circuit design method for wideband nonmagnetic absorbers at low microwave frequencies. *IEEE Transactions on Antennas and Propagation* 68(12), 1551–1558.
- Jain P, Singh AK, Pandey JK, Garg S, Bansal S, Agarwal M, Kumar S, Sardana N, Gupta N and Singh AK (2020) Ultra-thin metamaterial perfect absorbers for single-/dual-/multi-band microwave applications. *IET Microwaves Antennas Propagation* 14(5), 390–396.
- Li H, Yuan LH, Zhu B, Shen XP, Cheng Q and Cui TJ (2011) Ultrathin multiband gigahertz metamaterial absorbers. *Journal of Applied Physics* 110(1), 014909–1–014909–8.
- Kollatou TM, Dimitriadis AI, Assimonis SD, Kantartzis NV and Antonopoulos CS (2013) A family of ultra-thin polarization-insensitive, multiband, highly absorbing metamaterial structures. *Progress in Electromagnetics Research* 136, 579–594.
- Lee J, Yoo M and Lim S (2015) A study of ultra-thin single layer frequency selective surface microwave absorbers with three different bandwidths using double resonance. *IEEE Transactions on Antennas and Propagation* 63(1), 221–230.
- Joy V, Baghel S, Nazeer ST and Sing H (2023) Broadband, polarization-insensitive and ultra-thin metasurface-based radar-absorbing structure for radar cross-section reduction of planar/conformal hotspots. *Journal of Electronic Materials* 52, 6625–6636.
- Liujia E, Liu Z, Zhang J, Xu Z, Yuan Z, Mei Z and Niu T (2023) Realization of an ultra-thin absorber with fragmented magnetic structure at L-, S-, and partial C-bands. *Journal of Applied Physics* 134(22), 223105–1–223105–8.
- Wen J, Ren Q, Peng R and Zhao Q (2021) An all-dielectric metasurface absorber based on surface wave conversion effect. *Applied Physics Letters* 119(6), 062902–1–062902–7.
- Costa F, Genovesi S, Monorchio A and Manara G (2014) Low-cost metamaterial absorbers for sub-GHz wireless systems. *IEEE Antennas and Wireless Propagation Letters* 13, 27–30.
- Zhong S and He S (2013) Ultrathin and lightweight microwave absorbers made of mu-near-zero metamaterials. *Scientific Reports* 3, 2083–1–2083–5.
- Mishra N, Kumari K and Chaudhary RK (2018) An ultra-thin polarization independent quad-band microwave absorber-based on compact metamaterial structures for EMI/EMC applications. *International Journal of Microwave and Wireless Technologies* 10(4), 422–429.
- Yang X, Zhang X, Ding Z and Zhang Z (2023) Compact and ultra-thin absorber based on metasurface for multi-band energy absorption. *Optik* 273, 170478–1–170478–9.
- Almawani AHM, Srilatha K, Madhav BTP, Venkatesh B, Sravan CVSA, Rao MC and Alhwar ARH (2023) Dual band metasurface absorber with insensitive polarization and incidence angle for S and C band applications. *Journal of Communications Technology and Electronics* 68(11), 1371–1378.
- Kitahara KD, Suga R, Araki K and Hashimoto O (2019) Circular patch array absorber design for oblique incidence by using winding ratio model of transformer. *IEEE Transactions on Electromagnetic Compatibility* 61(1), 65–72.
- Chen J, Hu Z, Wang G, Huang X, Wang S, Hu X and Liu M (2015) High-impedance surface-based broadband absorbers with interference theory. *IEEE Transactions on Antennas and Propagation* 63(10), 4367–4374.
- Fu C, Zhang L, Liu L, Dong S, Yu W and Han L (2023) RCS reduction on patterned graphene-based transparent flexible metasurface absorber. *IEEE Transactions on Antennas and Propagation* 71(2), 2005–2010.
- Fu C, Zhang L, Zhang Y, Li N, Gu S, Ju J, Pan R, Liu X and Han L (2024) Bifunctional flexible metasurface based on graphene and vanadium dioxide for polarization conversion and absorption. *Diamond and Related Materials* 142, 110862–1–110862–11.
- Khan HA, Majeed A, Zahra H, Kakepoto FG, Abbas SM and Alathbah M (2024) Transparent conformal metasurface absorber for ultrawideband radar cross section reduction. *Journal of Physics D: Applied Physics* 57(13), 135105–1–135105–8.
- Fu C, Zhang X, Liu X and Han L (2023) RCS reduction of composite transparent flexible coding metasurface combined phase cancellation and absorption. *Optics Express* 31(17), 27365–27380.
- Erbulut DU, Masood SH, Tran VN and Sbarski I (2008) A novel approach of measuring the dielectric properties of PET preforms for stretch blow moulding. *Journal of Applied Polymer Science* 109(5), 3196–3203.
- Casula GA, Montisci G and Mazzarella G (2013) A wideband PET inkjet-printed antenna for UHF RFID. *IEEE Antennas and Wireless Propagation Letters* 12, 1400–1403.
- Koniczna M, Markiewicz E and Jurga J (2010) Dielectric properties of polyethylene terephthalate/polyphenylene sulfide/barium titanate nanocomposite for application in electronic industry. *Polymer Engineering & Science* 50(8), 1613–1619.
- Kirtania SG, Elger AW, Hasan MR, Wisniewska A, Sekhar K, Karacolak T and Sekhar PK (2020) Flexible antennas: A review. *Micromachines* 11(9), 847–1–847–43.

36. **Fan S, Suh W and Joannopoulos J** (2003) Temporal coupled-mode theory for the Fano resonance in optical resonators. *Journal of the Optical Society of America A* **20**(3), 569–572.
37. **Piper JR and Fan S** (2014) Total absorption in a graphene monolayer in the optical regime by critical coupling with a photonic crystal guided resonance. *ACS Photonics* **1**(4), 347–353.
38. **Isić G, Sinatkas G, Zografopoulos DC, Vasić B, Ferraro A, Beccherelli R, Kriezis EE and Belić M** (2019) Electrically tunable metal–semiconductor–metal terahertz metasurface modulators. *IEEE Journal of Selected Topics in Quantum Electronics* **25**(3), 8500108.
39. **Pozar DM** (1998) *Microwave Engineering*. Hoboken, NJ, USA: John Wiley and Sons, Inc., 4th Edn.
40. **Passia M-T and Yioultis TV** (2020) Fast analysis of metasurfaces through temporal coupled-mode theory. *IEEE Transactions on Magnetics* **56**(2), 7506804–1–7506804–4.
41. **Olk AE and Powell DA** (2019) Accurate metasurface synthesis incorporating near-field coupling effects. *Physical Review Applied* **11**(6), 064007–1–064007–10.
42. **Balanis CA** (1996) *Antenna Theory – Analysis and Design*. Hoboken, NJ, USA: John Wiley and Sons, Inc., 2nd Edn.
43. **Rozanov KN** (2000) Ultimate thickness to bandwidth ratio of radar absorbers. *IEEE Transactions on Antennas and Propagation* **48**(8), 1230–1234.
44. **Brandt R and Neuer G** (2007) Electrical resistivity and thermal conductivity of pure aluminum and aluminum alloys up to and above the melting temperature. *International Journal of Thermophysics* **28**(5), 1429–1446.
45. **Khanna Y and Awasti YK** (2020) Ultra-thin wideband polarization-insensitive metasurface absorber for aviation technology. *Journal of Electronic Materials* **49**(11), 6410–6416.
46. **Huang X, Pan K and Hu Z** (2016) Experimental demonstration of printed graphene nano-flakes enabled flexible and conformable wideband radar absorbers. *Scientific Reports* **6**, 38197–1–38197–8.
47. **Yoo M, Kim HK, Kim S, Tentzeris M and Lim S** (2015) Silver nanoparticle-based inkjet-printed metamaterial absorber on flexible paper. *IEEE Antennas and Wireless Propagation Letters* **14**, 1718–1721.
48. **Kalraiya S, Chaudhary RK, Abdalla MA and Gangwar RK** (2019) Polarization and incident angle independent metasurface absorber for X-band application. *Materials Research Express* **6**(4), 045802–1–045802–8.



Savvas I. Raptis received the Diploma degree in electrical and computer engineering from the Aristotle University of Thessaloniki, Thessaloniki, Greece, in 2015, where he is currently pursuing the Ph.D. degree. His research interests include the design of high-frequency microwave components for 5G and IoT communications, metamaterials, metasurfaces, and reconfigurable intelligent surfaces (RIS) modeling and design.



Konstantinos Ntokos received the Diploma degree in electrical and computer engineering from the Aristotle University of Thessaloniki in 2020, where he is currently pursuing the Ph.D. degree. His main research interests include computational methods in electromagnetics, design of metasurfaces, reconfigurable intelligent surfaces, metamaterials, and high-frequency microwave components.



Maria-Thaleia Passia received the Diploma degree and Ph.D. in electrical and computer engineering from the Aristotle University of Thessaloniki, Greece in 2015 and 2020, respectively. Her research interests include the design of metamaterial devices for microwave and millimeter-wave applications, as well as development of semi-analytical formulations for the fast synthesis of complex metasurface structures.



Konstantina Tourlouki, based in Athens, is a seasoned professional in micro and nanofabrication, with 4 years of experience. She holds a BSc in materials science and an MSc in applied optoelectronics, both from the University of Patras. Currently pursuing her Ph.D. at the same institution, Konstantina specializes in the fabrication of optical elements for security applications using advanced nanoimprint lithography and laser techniques. With extensive experience as a Photonics Engineer for 3 years, she brings a wealth of expertise to her role. Transitioning to her current position as a Research and Innovation Manager at Nanotypos, Konstantina continues to contribute to projects in micro/nanofabrication, optics, and biomedicine, advancing the development of high-performance products. Passionate about pushing the boundaries of nanotechnology, her career goal is to pioneer sustainable solutions with global impact.



Nikolaos Kehagias's research work focuses on the study and developed of novel nano-lithography and nano-patterning techniques for the fabrication of 2D and 3D structures. The combination of top-down and bottom-up imprint based lithography techniques with novel materials are investigated to create nano enabled functional surfaces and components. In particular, interest is the fabrication of passive nano-photonic surfaces which could manipulate light in two and/or three dimensions. Efforts have been employed in developing high throughput nano manufacturing processed suitable to process hybrid materials for the realization of and biomimetic surfaces. A major goal is to transfer new technological discoveries to industrial applications.



Emmanouil E. Kriezis received the Diploma degree in electrical engineering and the Ph.D. degree from the School of Electrical and Computer Engineering, Aristotle University of Thessaloniki, Thessaloniki, Greece, in 1991 and 1996, respectively. He joined the Department of Engineering Science, University of Oxford, Oxford, U.K., in 1998, initially as an Engineering and Physical Sciences Research Council Post-Doctoral Researcher, and later in 2001 he received the prestigious Royal Society University Research Fellowship to study light propagation in complex anisotropic media. Since 2004, he has been Professor of optical and microwave communications at the School of Electrical and Computer Engineering, Aristotle University of Thessaloniki. His current research interests include nonlinear effects at optical frequencies, plasmonics, silicon photonics, graphene devices, and metasurfaces.



Traianos V. Yioultsis (M'09) received the Diploma degree in electrical engineering and Ph.D. degree in electrical and computer engineering from the Aristotle University of Thessaloniki (AUTH), Thessaloniki, Greece, in 1992 and 1998, respectively. From 1993 to 1998, he was a Research and Teaching Assistant in the Department of Electrical and Computer Engineering, AUTH. From 2001 to 2002, he was a Postdoctoral Research Associate

in the Department of Electrical and Computer Engineering, University of Illinois at Urbana-Champaign, Urbana, IL, USA. Since 2002, he has been with the Department of Electrical and Computer Engineering, AUTH, where he is currently a Professor. His current interests include the analysis and design of microwave/photonic circuits and antennas with fast computational and optimization techniques and the modeling of complex wave propagation problems.